Chapter 29
Multiscale Evaluation of Satellite Precipitation Products: Effective Resolution of IMERG

Clément Guilloteau and Efi Foufoula-Georgiou

Abstract Satellite precipitation products are essential for global analysis of water cycle dynamics as well as for regional analyses in regions where no ground observations are available. For any climatic or hydrologic application, it is important to know down to which scale a gridded satellite precipitation product can accurately resolve the spatial patterns of precipitation. This scale, which we call "effective resolution", is a complex combination of the instrument resolution (especially so for multisensor products such as IMERG), the multi-sensor retrieval or merging algorithm, and the type of the precipitating system, and it can differ substantially from the grid size of the satellite product. Here, we use a wavelet-based framework to quantitatively define the effective resolution of the IMERG multi-satellite product by comparison with the MRMS ground radar product at the hourly time scale over the continental United States. Our findings show that the effective resolution varies across geographical areas, seasons and types of precipitation and provide insight for the use of those products in hydrologic applications and for algorithmic improvements.

Keywords Precipitation · Rainfall · Evaluation · Validation · Error modeling · GPM · Raingauges · Nominal resolution · Effective resolution · Spectral analysis · Wavelets

C. Guilloteau (✉)
Department of Civil and Environmental Engineering, University of California, Irvine, CA, USA
e-mail: cguillot@uci.edu

E. Foufoula-Georgiou
Department of Civil and Environmental Engineering, University of California, Irvine, CA, USA

Department of Earth Science, University of California, Irvine, CA, USA

V. Levizzani et al. (eds.), *Satellite Precipitation Measurement*, Advances in Global Change Research 69, https://doi.org/10.1007/978-3-030-35798-6_5

29.1 Introduction

IMERG (Integrated Multi-Satellite Retrievals for GPM, Huffman et al. 2015) is the operational quasi-global multi-satellite quantitative precipitation estimation product (QPE) of the NASA Global Precipitation Measurement (GPM) program. IMERG V05 is provided on a spatial grid covering the globe from latitude 60°N to latitude 60°S with a 0.1° latitude and longitude increment, and a temporal sampling of 30 min. It strives to resolve the sub-mesoscale patterns of precipitation, which typically requires a resolution of a few km or a few dozen km. Obviously, a fine grid increment is necessary for such purpose. But in fact, although the grid increment is often referred to as the product's "resolution" (or "nominal resolution"), there is no guarantee that the precipitation patterns are actually resolved down to the finest scale allowed by the grid. The IMERG estimates rely on the measurements of a dozen different instruments in the microwave and infrared domains. The spatial resolution of these instruments varies from 70 km (SSM/I at 19 GHz) to 2 km (Himawari-8 infrared channels). Given this, it is a-priori uncertain which scales can be resolved by the IMERG algorithm. Moreover, the performance of IMERG at various scales is expected to vary because of the irregular temporal sampling from the different instruments, the evolving configuration of the GPM constellation and the climatic spatial and temporal variability. One must also consider the potential filtering effects associated with the retrieval procedure of each instrument and with the merging procedure.

The question of the "effective resolution" of numerical weather prediction models has been raised several times in the literature (e.g., Pielke 1991; Grasso 2000) and is typically assessed by comparison with observations in the Fourier spectral domain (Skamarock 2004; Frehlich and Sharman 2008; Wong and Skamarock 2016), or in a wavelet spectral domain (Bousquet et al. 2006; Vasić et al. 2007). For numerical models, the assessment of the effective resolution consists of verifying if the output fields show the right spectral energy at all frequencies or scales. The effective resolution is quantified as the finest scale (or highest frequency) for which the power spectrum of the modelled field matches the power spectrum of the observed field. However, the agreement of the power spectra does not guarantee the agreement of the two fields in terms of the spatial location of the observed patterns. In this paper, the effective resolution of IMERG is assessed by comparison with the MRMS gauge-adjusted radar QPE over the Contiguous United States (CONUS) in the wavelet scale domain, which in contrast to the Fourier analysis provides a localised assessment. Moreover, in addition to the wavelet power spectra of the two fields, the spectrum of their difference and the correlation of the local wavelet coefficients of the two fields at various scales are analysed and used in defining the effective resolution.

29.2 Data

29.2.1 IMERG

IMERG is the quasi-global time-continuous precipitation product of the NASA GPM program. To allow time-continuous coverage IMERG combines the observations of a dozen passive microwave and infrared sensors. The algorithm implements the CMORPH Kalman filter approach (Joyce and Xie 2011) to dynamically merge the various instantaneous passive microwave and infrared precipitation fields. It is therefore labelled as a level-three product. The PERSIANN-CCS (Hong et al. 2004) and GPROF (Kummerow et al. 2015) algorithms are used to respectively retrieve the instantaneous infrared and microwave precipitation fields (level two products) on which IMERG relies. The product's grid resolution is 0.1° and the temporal sampling is 30 min. In this study, the Final IMERG product (v5), which includes model-based corrections and gauge adjustment is evaluated at the hourly scale.

29.2.2 MRMS Gauge-Adjusted Radar QPE

The NOAA Multi-Radar Multi-Sensor system (Zhang et al. 2016) integrates the data from 176 radars and more than 7000 automatic rain gauges over CONUS and Southern Canada to generate a suite of precipitation estimation products. The product used in this study as a reference for the evaluation of IMERG is the 1-h MRMS gauge-adjusted radar QPE. The MRMS gauge-adjusted QPE has a native grid increment of 0.01°. It is aggregated here at 0.1° to be compared with IMERG. In spite of the large number of radars composing the MRMS network, some areas remain poorly covered. Figure 29.1 shows the MRMS radar quality index, which is a function of the distance to the closest radar and also takes into account the beam blockage from the relief (Zhang et al. 2016). In this study, only the pixels (at 0.1°) for which the quality index is higher than 0.5 are retained. For the computation of some specific scores a higher threshold is retained (e.g., Fig. 29.4).

29.3 Method: Spectral Analysis in the Wavelet Domain

29.3.1 Rationale

Many studies have demonstrated that the performance of satellite estimation products strongly depends on the spatial and temporal scales at which they are evaluated (Hossain and Huffman 2008; Turk et al. 2009; Sohn et al. 2010; Scheel et al. 2011). When evaluated at spatio-temporal scales approaching their full nominal resolution, finely-gridded products may show mediocre performances, to the point that the

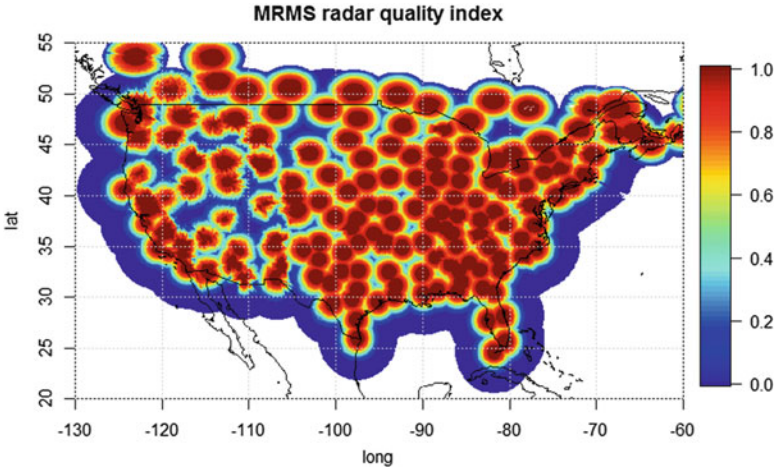

Fig. 29.1 MRMS radar quality index. The quality index considers the distance to the closest radar and the beam blockage by the relief (see Zhang et al. 2016 for the definition of the quality index)

variance of the retrieval error may be in the same order of magnitude as the statistical variance of the reference precipitation (Shen et al. 2010; Haile et al. 2013; Rios Gaona et al. 2016). Under the hypotheses that the retrieval error is purely random, has a zero expected value and is independent from one pixel to another (i.e., is spatially and temporally independent), its variance naturally decreases through spatial and temporal averaging with a N^{-1} decrease rate, where N is the number of averaged individual estimates (i.e., number of averaged pixels). However, these hypotheses, are generally not verified, particularly the hypothesis of spatial and temporal independence of the error. With correlated errors, the decrease rate of the error variance is significantly slower (von Storch 1999; Hossain and Anagnostou 2006). This makes necessary to evaluate precipitation products at multiple scales.

The validation of satellite products is typically performed by comparison with a trusted reference dataset. The most straightforward way to perform the multiscale evaluation is to coarsen the compared fields by aggregation at multiple scales and to perform a complete analysis at each scale (Turk et al. 2009; Sohn et al. 2010; Scheel et al. 2011). However, this analysis is highly redundant: all the information contained in the coarse-resolution fields is necessarily present in the fine-resolution fields too. This can make the interpretation of the multiresolution scores ambiguous. For example, if the retrieval performance appears to be identical at all scales there may be two different explanations: (1) The product performs identically well at capturing fine-scale and coarse-scale variations. (2) The fine-scale (high-frequency) variations are negligible compared to the coarse-scale (low-frequency) variations in both the evaluated product and the reference dataset; in that case the high-resolution fields and low-resolution fields are in fact very similar (the high-resolution fields being simply “oversampled” versions of the low-resolution ones) and the retrieval of the fine-scale variations is not really evaluated.

The spectral analysis in the Fourier domain or wavelet domain allows us to decompose the fields into several frequency bands or several scales and to analyse them independently. While the multi-resolution analysis by successive coarsening can be seen as equivalent to analysing the fields through a suite of low-pass spatial filters, the spectral analysis can be seen as equivalent to analysing the fields through a suite of band-pass filters. The essential question we want to answer through the spectral analysis is: "what supplementary information does the fine-resolution fields contain relatively to the coarse resolution fields?". We chose here to perform the spectral analysis in the wavelet scale domain, using the two-dimensional discrete orthogonal Haar wavelet decomposition. This choice is guided by the fact that: (1) The wavelet coefficients are interpretable as local differences or as local gradients. In particular, the Haar wavelet coefficients are simply computed as the difference between the spatially averaged values of the analysed variable (here precipitation rate) in two adjacent rectangular areas. (2) Unlike the Fourier coefficients, the wavelet coefficients are spatially localised, allowing to study the spatial variations of the spectral properties of the fields. This in particular overcomes the issue of spatial and temporal non-stationarity of the precipitation fields. (3) With the discrete orthogonal wavelet decomposition, the wavelet coefficients are spatially uncorrelated and uncorrelated across scales. Because of this, the wavelet power spectrum, which is simply the statistical variance of the wavelet coefficients as a function of the scale, is unambiguous. Weniger et al. (2017) provides a review on the use of wavelet transforms for spatial verification.

The discrete orthogonal wavelet decomposition is performed as an iterative process over a finite number of levels corresponding to dyadically increasing spatial scales. At the first level, the original field is decomposed into one coarse-scale component (smoothing coefficients) obtained by convolution of the field with a low-pass spatial filter, and three fine-scale components (wavelet coefficients) obtained by convolution of the field with high-pass directional filters (see Appendix). The fine-scale components are retained and the coarse-scale component is further decomposed at the second level, etc. At the end, since the decomposition has a finite number of levels, one residual coarse-scale component must be retained along with the wavelet coefficients at all scales to allow the reconstruction of the original field. The low-pass filter used for the Haar decomposition is a simple rectangular averaging filter (see Appendix A). Consequently, analysing the Haar smoothing coefficients would be strictly equivalent to a multi-resolution analysis by successive aggregations. Instead, we analyse the high-pass wavelet coefficients at each scale. In fact, the Haar wavelet coefficients at scale λ contain exactly the information that is lost when the field is coarsened by averaging from the resolution λ to the resolution $2 \times \lambda$. Because there is no redundancy of information across scales in the wavelet coefficients space, the spatial variations at each scale can be evaluated independently. We can therefore actually estimate the added value of a high-resolution field relatively to the same field at a coarser resolution in terms of information content.

In this article, the "information content" is quantified through the statistical variance or energy (i.e., sum of the squared values) of the original fields and of the

wavelet coefficients. In information theory, the "information content" is classically quantified through the Shannon entropy. One could analyse the Shannon entropy and mutual information of the wavelet coefficients (Starck et al. 1998; Labat 2005; Labat et al. 2005). However, we chose here to rather use the variance and covariance metrics because we also analyse the error field and its wavelet decomposition. The Shannon entropy depends of the probability of observing a given value in the field but ignores the numerical value itself. Therefore, the Shannon entropy of the error field would ignore the amplitude of the errors (Petty 2018).

29.3.2 Implementation

The IMERG and MRMS hourly precipitation fields at 0.1° (about 10 km) are decomposed through a two-dimensional discrete orthogonal decomposition with the Haar wavelet. The decomposition is performed at six levels, with resulting dyadic scales being 10, 20, 40, 80, 160 and 320 km. The residual low-pass component of this decomposition is the original field smoothed at the 640 km spatial resolution. We analyse the wavelet coefficients of IMERG and MRMS at each scale in terms of their variance (or energy) and covariance as well as the variance of their difference. The orthogonal wavelet decomposition is energy conservative, i.e. the sum of the energy of the wavelet coefficients at all dyadic scales plus the energy of the residual low-pass component equals the energy of the original field. Because the wavelet decomposition is a linear operation, the wavelet coefficients coming from the decomposition of the difference of the two fields are equal to the difference of the wavelet coefficients of the two fields. Consequently, the squared difference between the two fields equals the sum of the spectral energy of the difference of their wavelet coefficients at all scales plus the energy of the difference of their low-pass components.

We noted previously that, in two dimensions, three series of directional wavelet coefficients are produced at each scale. The first two series of coefficients encode the variation of the field along the vertical (North-South) and horizontal (East-West) direction. The third series of coefficients, sometimes referred to as the "diagonal" coefficients encodes the coupling between the horizontal and vertical variations (see appendix). One can analyse the three series independently, which allows characterising anisotropic features in the fields (Kumar and Foufoula-Georgiou 1993; Kumar 1995; Perica and Foufoula-Georgiou 1996). Here, the three series of coefficients are not differenced, and the spectral energy at each scale is computed as the sum of the energy of the three series of coefficients. The discrete wavelet energy spectrum (or power spectrum) $S(y,\lambda)$ of the field y shows the energy (or variance) of the wavelet coefficients as a function of the scale λ.

Besides comparing the energy spectra of MRSM and IMERG and analysing the spectrum of their difference, we also analyse the linear correlation and covariance between the wavelet coefficients of the two precipitation fields. We note that at each scale λ, the correlation of the wavelet coefficients is related to the spectral energies:

$$Wcor(y_1, y_2, \lambda) = \frac{CS(y_1, y_2, \lambda)}{\sqrt{S(y_1, \lambda)\, S(y_2, \lambda)}} \tag{29.1}$$

and

$$2 \times CS(y_1, y_2, \lambda) = S(y_1, \lambda) + S(y_2, \lambda) - S(y_2 - y_1, \lambda) \tag{29.2}$$

where $Wcor(y_1, y_2, \lambda)$ is the linear correlation between the wavelet coefficients of the y_1 and y_2 fields as a function of the scale λ; and $CS(y_1, y_2, \lambda)$ is the cross-spectrum of y_1 and y_2, i.e. co-spectral energy (sum of the products of the wavelet coefficients) of y_1 and y_2 as a function of λ.. The first relation is true because the expected value of the wavelet coefficients at any scale is equal to zero.

Our analysis aims at determining at which scales the spatial variations of precipitation are actually resolved by the IMERG product. The following criterion is chosen to assess the effective resolution. The scale λ is considered resolved if:

$$S\left(y_{retr} - y_{ref}, \lambda\right) < 0.5 \times S\left(y_{ref}, \lambda\right) \tag{29.3}$$

i.e. if the spectral energy of the error is less than half the spectral energy of the reference field. Here, y_{retr} denotes the evaluated retrieved precipitation field (IMERG in our case) and y_{ref} the reference precipitation field (MRMS in our case). The effective resolution is the finest resolved scale.

29.3.3 Illustrative Case Study

Figure 29.2 shows the 1-h cumulative IMERG and MRMS precipitation fields over the South-Eastern part of CONUS on 30 Nov. 2016 from 0400 to 0500 UTC, along with the error field (IMERG-MRMS). The Haar wavelet power spectrum of the three fields is shown on the last panel. One can see that the IMERG precipitation field is smooth compared to the MRMS field, specifically, it does not reproduce the fine-scale structures and sharp transitions observed in the MRMS field. Small very active cells, showing precipitation rates between 35 and 50 mm h^{-1} are observed in the MRMS field but not in the IMERG field. Consequently, while the two fields have about the same average hourly precipitation amount (0.60 mm for MRMS and 0.57 mm for IMERG), for the MRMS field, precipitation is concentrated in a smaller area (in the MRMS field, 60% of the precipitation is concentrated in a 50,000 km^2 area, while in the IMERG field, 60% of the precipitation is concentrated in an 80,000 km^2 area). These characteristics are reflected on the wavelet power spectrum: the IMERG field shows a deficit of energy (i.e., spatial variability) at scales finer than 160 km. The wavelet coefficients are also poorly correlated at fine scales. For example, at scales of 10 and 20 km the linear correlations between IMERG and MRMS wavelet coefficients are 0.15 and 0.36, respectively. One direct consequence

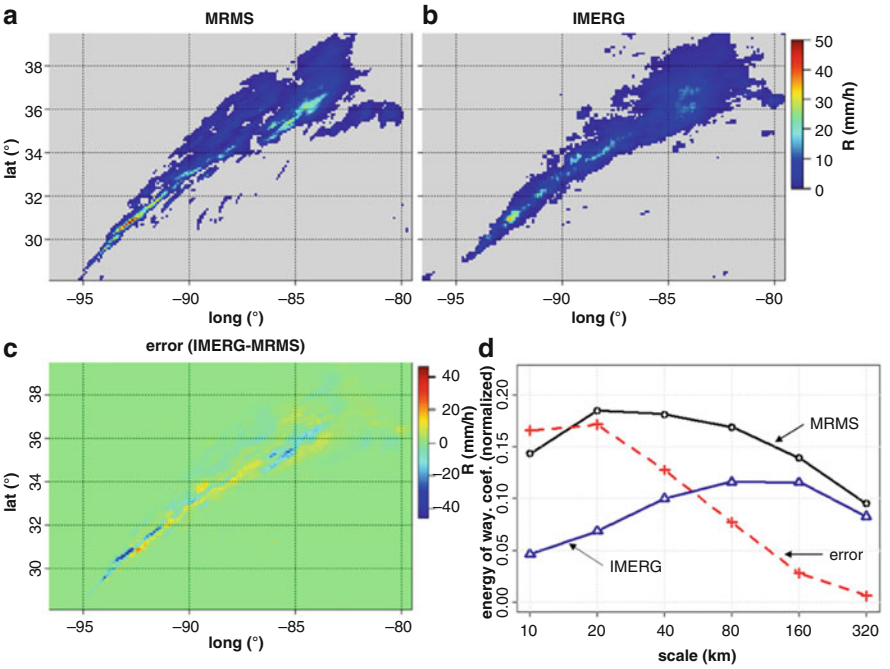

Fig. 29.2 (**a**) MRMS hourly precipitation over South-Eastern US, on 30 Nov. 2016 from 0400 to 0500 UTC. (**b**) Corresponding IMERG hourly precipitation. (**c**) IMERG error relative to MRMS. (**d**) Wavelet energy spectra of MRMS (thick black line with circles), IMERG (thick blue line with triangles) and of the error IMERG-MRMS (dashed red line with crosses). The energy spectra are normalised by the total energy (sum of squared values) of the MRMS field

of this is the high spectral energy of the error at these scales. The spectrum of the error reveals that 94% of the squared error is explained by the misrepresentation of the spatial variations at scales finer than 160 km (and 58% only for the scales finer than 40 km). Applying criterion (29.3), the effective resolution is found to be close to 80 km for this case study.

29.4 Results

The approach described previously is extended over CONUS to analyse the performance of IMERG over a complete year (November 2016 to October 2017). The cold season (November–April) and warm season (May–October) are separated for the analysis. Figure 29.3 shows the cumulative precipitation of IMERG and MRMS for both periods. The cumulative precipitation fields are smoothed using a 640 km sliding window averaging to preserve only the coarse-scale patterns. One can see that IMERG and MRMS show similar patterns, but also that IMERG notably

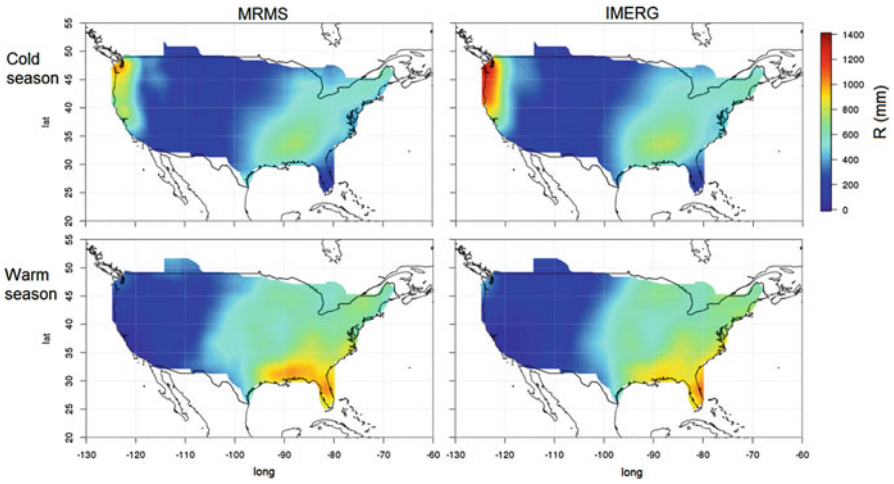

Fig. 29.3 Seasonal cumulative precipitation from Nov. 2016 to Apr. 2017 (cold season) and May – Oct. 2017 (warm season) for MRMS and IMERG. The fields are spatially smoothed through sliding window averaging with a 640 km wide window (corresponding to the smoothing function associated with the Haar wavelet)

(relatively) overestimates the cumulative precipitation amount in the North-West region along the Pacific Coastline during the cold season. For each period, the wavelet power spectra of the hourly IMERG and MRMS fields and of the error field are cumulated at every time step. Figure 29.4 shows the cumulative spectra. One can see that, the power spectra of IMERG and MRMS are relatively close even if IMERG slightly overestimates the amplitude of the spatial variations at the 80–160 km scales for the cold season, and underestimates the amplitude of the spatial variations at scales finer than 80 km during the warm season. The MRMS cold season and warm season spectra show notable differences. The spectral energy of MRMS is maximal around 40~80 km during the cold season and around 20~40 km during the warm season. These scales correspond to the typical dimension of the most prominent structures observed in the MRMS hourly precipitation fields during the two periods. For IMERG, the maximum of energy is found consistently around 80 km for both seasons: the IMERG spectrum shows less seasonal variations than the MRMS spectrum.

The mean squared difference between IMERG and MRMS fields is 1.16 times the mean squared value (power) of MRMS during the cold season and 0.83 times the mean squared value of MRMS during the warm season. These numbers may appear very high; however, Fig. 29.4 shows that the ratio of the spectral energy of the error over the spectral energy of the MRMS reference varies considerably across scales. During the warm season, the spectral energy of the error increases with finer scales. During the cold season, the spectral energy of the error peaks at the 40 km scale. At the 10 and 20 km scales, the spectral energy of the error is systematically higher than the spectral energy of MRMS, meaning that erasing the fine-scale variation in

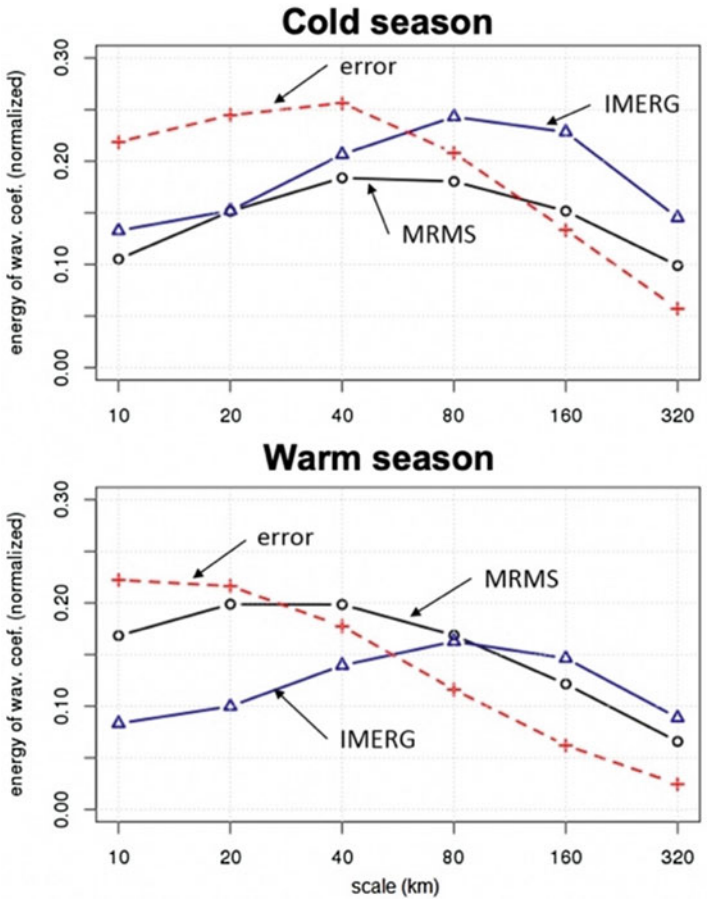

Fig. 29.4 Average wavelet energy spectra of MRMS (black line with circles), and IMERG (blue line with triangles) hourly precipitation fields and of the error IMERG-MRMS (dashed red line with crosses), computed over CONUS Nov. 2016 – Apr. 2017 (cold season) and May – Oct. 2017 (warm season). The spectra are computed at each time step and summed over the analysed period. The energy spectra are normalised by the total energy (sum of squared values) of the MRMS fields. Only the pixels with a MRMS radar quality index >0.9 are retained for the computation of the spectra

IMERG (e.g., using a sliding window averaging to smooth the field) would reduce the mean squared difference between IMERG and the 10 km resolution MRMS fields. The scales 10 and 20 km contribute together 40% of the total squared error during the cold season and 53% during the warm season. The scales 40 and 80 km contribute together 40% of the total squared error during the cold season and 35% during the warm season. Applying the criterion (29.3), we find an effective resolution around 160 km over CONUS during the warm season. During the cold season, the spectral energy of the error is relatively high at all scales, and not even the 320 km scale is resolved according to criterion (29.3). However, the spectra in Fig. 29.4 are averaged over various climatic zones, including mountainous areas,

and over 6-month periods during which various types of precipitation systems occur (including snow storms and hail which are known to be challenging in terms of satellite retrieval). A local precipitation feature can significantly affect the CONUS-averaged spectra. For example, the overestimation of precipitation in the North-West is essentially the reason why IMERG shows more spectral energy than MRMS at all scales during the cold season. The energy spectra, because they are quadratic measures are strongly influenced by extreme values in the fields (same is true for the mean squared error and the linear correlation), and consequently a few extreme precipitation events may have a strong influence on the computed statistics. A more detailed analysis is therefore necessary.

The spatial localisation of the wavelet coefficients allows to study the spatial variations of the spectral properties of the fields, and to perform a detailed regionalised analysis over CONUS. Figure 29.5 shows as a map the local ratio of IMERG spectral energy over MRMS spectral energy for all dyadic scales between 10 and 320 km. Overestimation by IMERG of the spectral energy at scales finer than 320 km is observed in particular in the North East during the cold season. During the warm season, IMERG overestimates the spatial variability at all scales along the Pacific Coast. The ratio between IMERG and MRMS spectral energy is close to 1 at all scales in the East during the warm season and in the South East during the cold season, demonstrating the agreement between MRMS and IMERG energy spectra in these regions. Strong underestimation by IMERG of the spatial variability at scales finer than 80 km is observed around $-100°$W and 30°N (between Texas and New Mexico) during the cold season, over the South-West (excluding coastal areas) during the warm season and locally along the Canada-US border during both seasons. For the 80 km scale and finer scales, a dependence on the distance to the closest ground radar can be observed: the apparent underestimation of the spatial variability by IMERG increases when the distance to the radar decreases. This is explained by the fact that the radar can better capture the fine-scale variability at shorter ranges. For Fig. 29.4 only the pixels with a quality index higher than 0.9 (i.e., pixels close to a ground radar) have been retained to mitigate this effect.

Figure 29.6 shows the regionalised ratio between the spectral energy of the error and the spectral energy of the MRMS reference. For the scales 40 km and coarser, a ratio lower than 1 is found in most areas (except locally, along coastal areas and along the US-Canada border) during the warn season. This is also true in the South-East during the cold season. In contrast, the spectral energy of the error is larger than the spectral energy of the reference at all scales in the North and over the Rocky Mountains for the cold season. This is likely related to the presence of frozen precipitation during winter in these regions, which is challenging for both the radar reference and the satellite retrieval. During the warm season, the highest relative error is found at all scales along the Pacific coastline. However, one must note that the Pacific coastline (and in particular its southern portion) is exposed to an extremely low amount of precipitation during the warm season (Fig. 29.3); therefore, even if the relative errors are large their absolute amplitude is very low. Figure 29.7 shows the local linear correlation coefficients between IMERG and MRMS wavelets coefficients at all scales. The patterns mostly follow the patterns shown in Fig. 29.6,

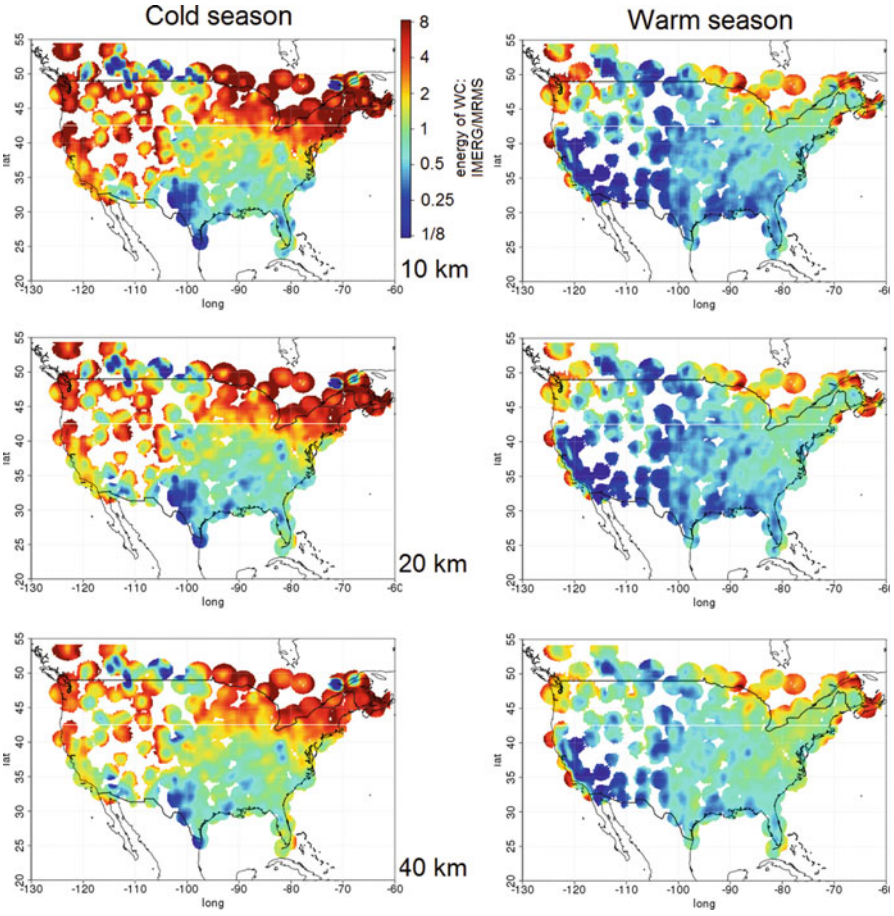

Fig. 29.5 Ratio of the spectral energy of IMERG hourly precipitation fields over the spectral energy of MRMS hourly precipitation fields during the cold and warm seasons. The spectral energies are computed at each time step and summed. A ratio close to one at all scales indicates the agreement of the IMERG and MRMS wavelet energy spectra

high correlation of the wavelet coefficients corresponding to low spectral energy of the error. Nevertheless, one will note that, particularly during the cold season, the spectral energy of the error at scales 320 and 160 km along the north part of the Pacific coastline is high in spite of the relatively good correlation of the wavelet coefficients at these scales. This shows that, in this region, the error mostly comes from a systematic bias: the amplitude of the spatial variations of the precipitation fields is systematically overestimated, which comes directly from the overestimation of the cumulative precipitation in winter in this region. Figure 29.8 shows the local effective resolution of IMERG, estimated using criterion (29.3). During the cold season, the effective resolution is generally found between 80 and 320 km in the

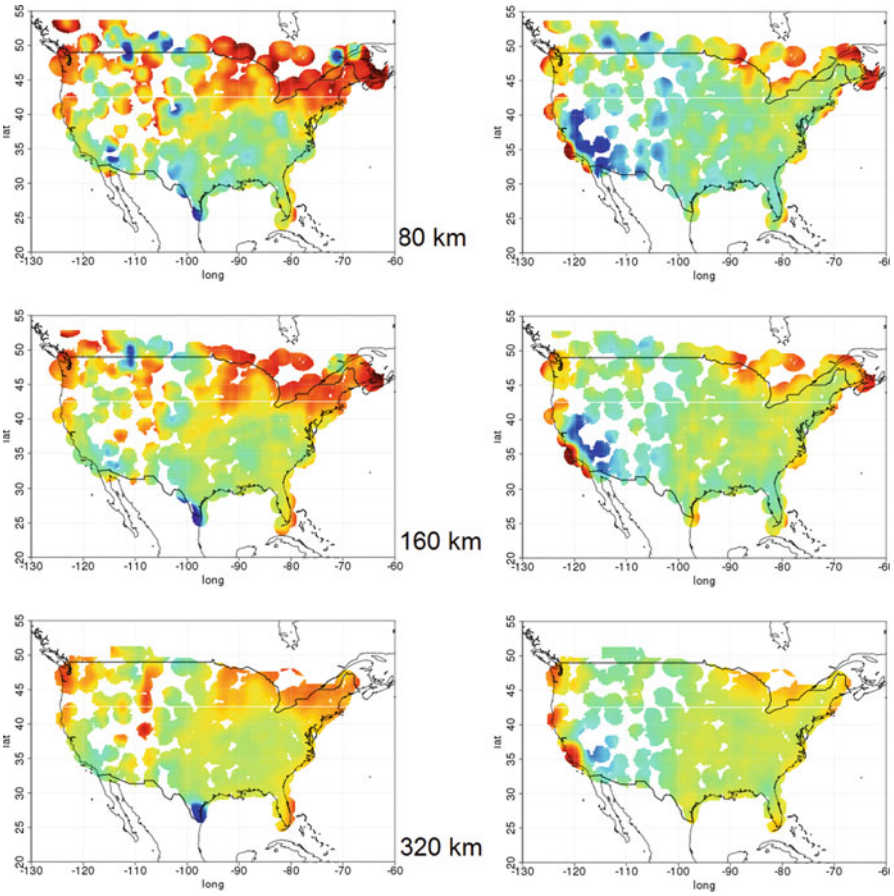

Fig. 29.5 (continued)

South-East and in the southern part of California, and locally between 40 and 80 km. In contrast, an effective resolution coarser than 320 km is found in the northern regions and over the mountains. During the warm season, the effective resolution is found finer than 160 km over most of CONUS, between 160 and 320 km in North-West and over the mountains, and coarser than 320 km in the northernmost regions. Coastal areas appear to be challenging, with an effective resolution generally coarser than 320 km during both seasons, except for the Northern coastline of the Gulf of Mexico where the performance of IMERG is remarkably good even at the 40~80 km scales.

Figure 29.9 shows the averaged spectra of IMERG, MRSM and of the error during the cold season computed only over the South-Eastern region where the effective resolution is finer than 160 km. The cold-season spectra in the South-East are similar to the all-CONUS warm season spectra. During the warm season and also

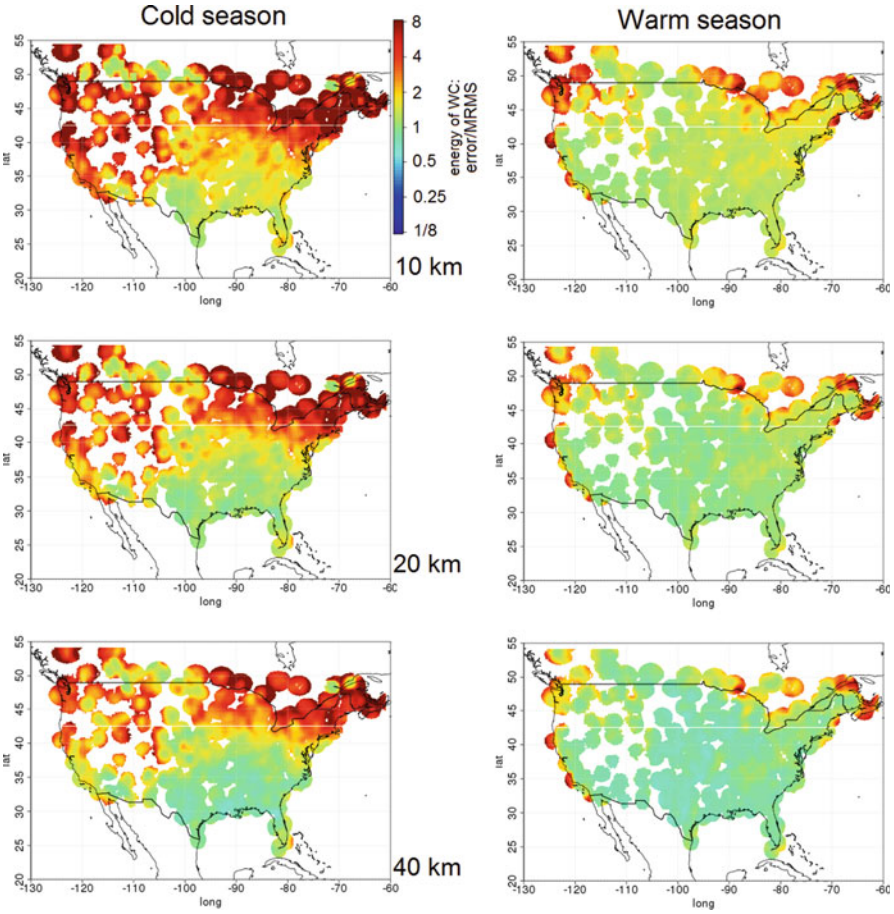

Fig. 29.6 Ratio of the spectral energy the IMERG hourly error (i.e., IMERG-MRMS) over the spectral energy of MRMS hourly precipitation during the cold and warm seasons. The spectral energies are computed at each time step and summed. A low spectral energy of the error indicates the agreement between IMERG and MRMS spatial patterns (gradients) at the corresponding scale

during the cold season in the South-West IMERG slightly underestimates the spatial variability of precipitation at scales finer than 80 km but the IMERG spectrum still shows substantial spectral energy at scales 10–40 km. This shows that IMERG hourly precipitation fields are not dramatically smoother than the MRMS hourly precipitation fields. Consequently, the high value of the spectral energy of the error at scales finer than 80 km is not caused by the absence of information in the IMERG fields at these scales but is rather due to the fact that this information does not match the information in the MRMS fields at the same scales. Both IMERG and MRMS fields show substantial fine-scale patterns but these patterns are different: they may be spatially shifted, oriented in different directions or completely independent.

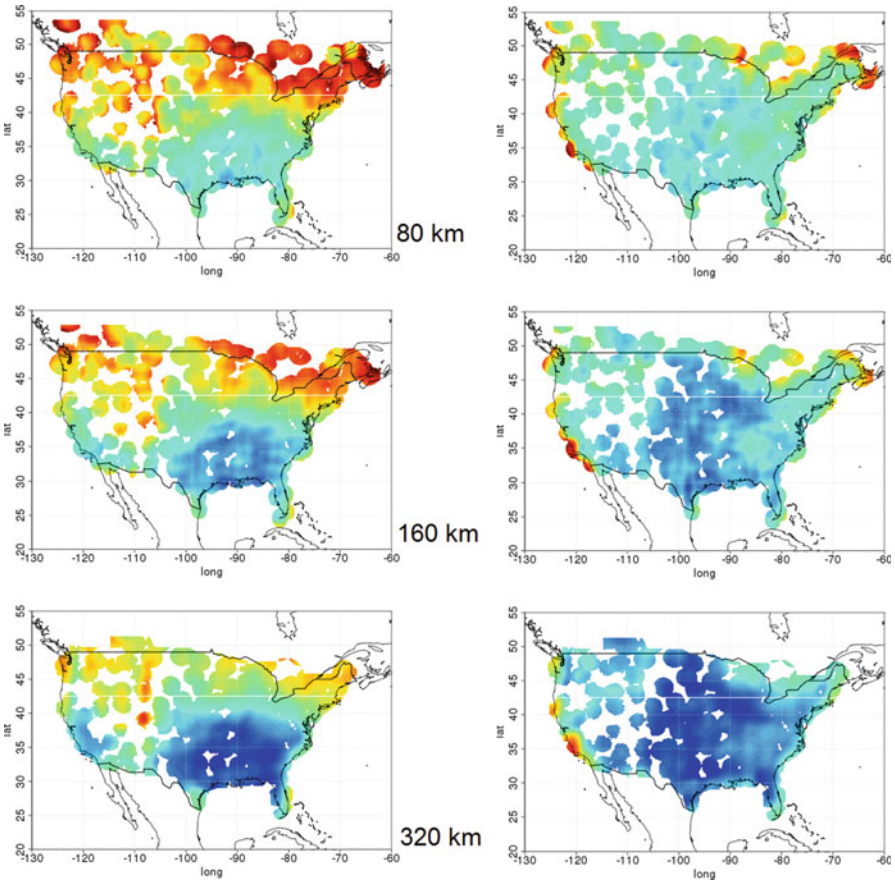

Fig. 29.6 (continued)

29.5 Conclusions

The performed spectral comparison of IMERG and MRMS hourly cumulative precipitation reveals that over the continental United States IMERG can resolve scales down to 40~80 km. However, in certain areas, and particularly where frozen precipitation is present, the retrieval of spatial variations of precipitation at scales between 80 and 320 km can be challenging for IMERG. The spatial variability a scales 640 km and larger scales was not evaluated against the radar because only a few geographical areas with such large dimensions are continuously covered by the MRMS radar network.

The wavelet energy spectra of IMERG and MRMS show generally little difference. IMERG shows a maximum of energy at a coarser scale than MRMS (around 80 km for IMERG and around 20 or 40 km for MRMS depending on the season). For regions and seasons dominated by frozen precipitation, IMERG appears to slightly

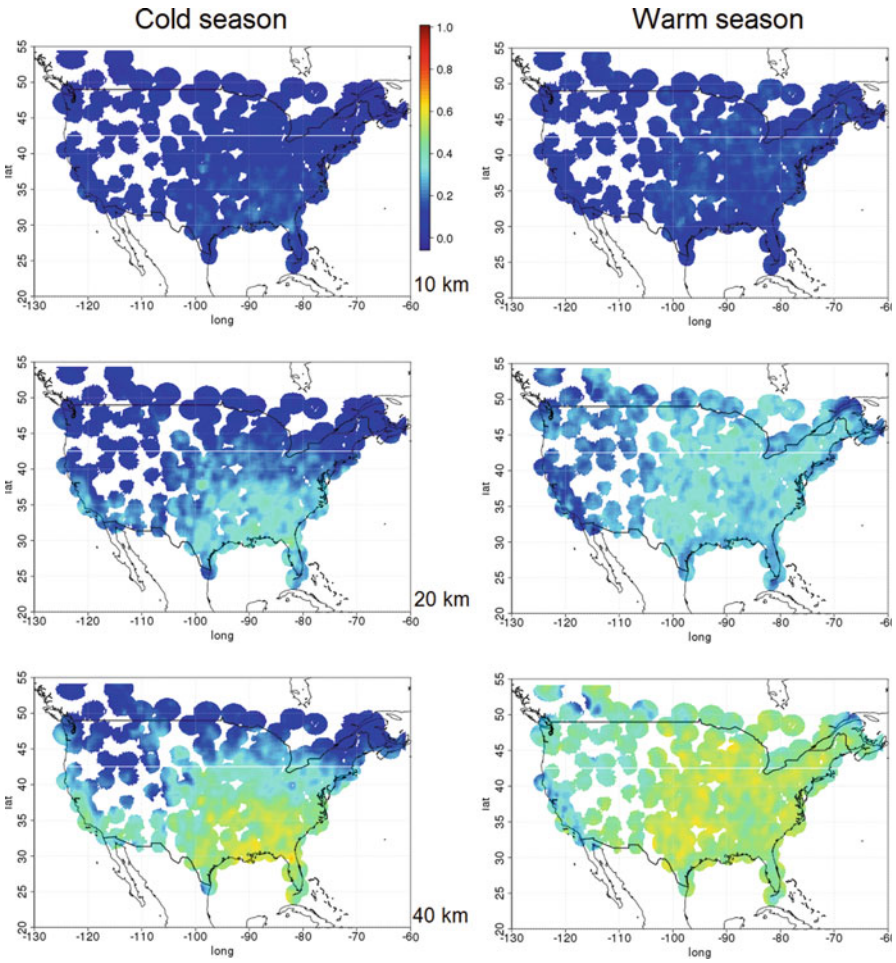

Fig. 29.7 Linear correlation between the wavelet coefficients of the IMERG and MRMS hourly precipitation fields. A high correlation of the wavelet coefficients indicates the agreement between IMERG and MRMS spatial patterns (gradients) at the corresponding scale. Contrary the spectral energy of the error, the correlation is not sensitive to potential biases in the magnitude of the wavelet coefficients

overestimate the amplitude of the spatial variation of the precipitation rates at scales between 80 and 320 km. When liquid precipitation is dominant, IMERG tends to slightly underestimate the spatial variability of precipitation at scales finer than 80 km, producing marginally smoother fields than MRSMS. The error field systematically shows high spectral energy at scales finer than 80 km, sometimes higher than the spectral energy of the radar reference. This is caused by the fact that the fine-scale variations of the IMERG fields do not match the variations of MRMS as revealed by

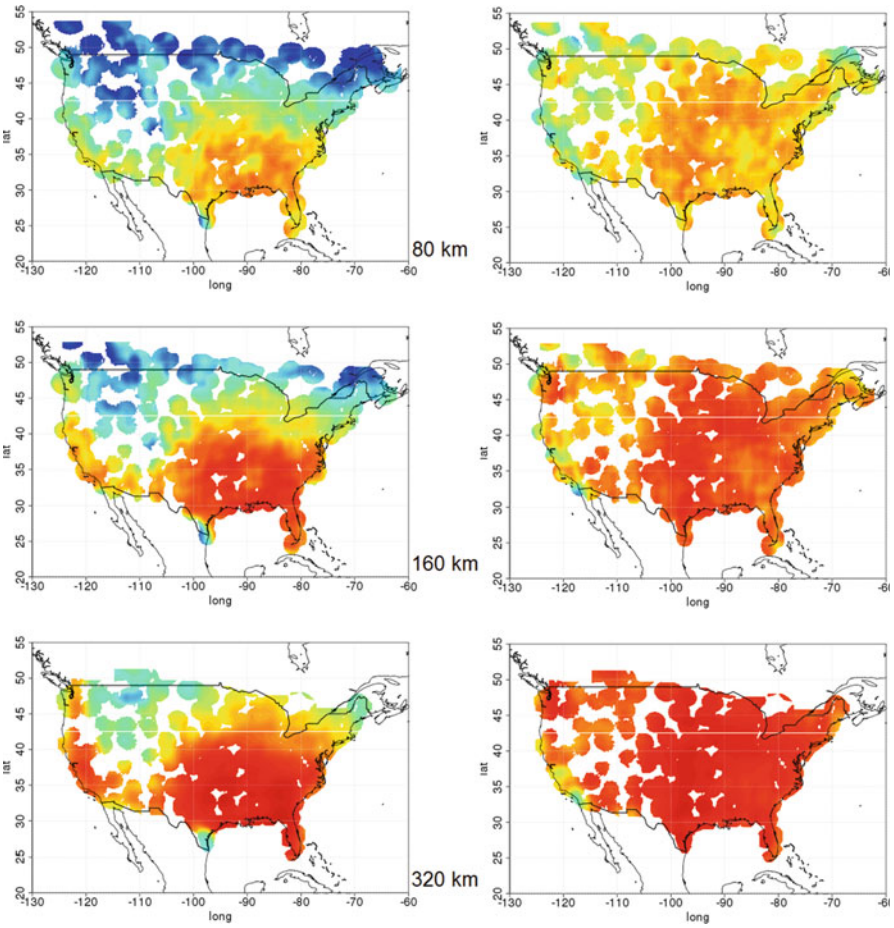

Fig. 29.7 (continued)

the low correlation of the wavelet coefficients. During the warm season, the spectral energy of the error is more concentrated in the fine scales than during the cold season: scales coarser than 40 km account for only 25% of the total squared error during the warm season (against 40% during the cold season).

We note that, while the gradients of IMERG and MRMS at scales finer than 80 km do not generally match, they are still statistically similar (in terms of variance of the wavelet coefficients). Considering that the IMERG merging algorithm relies on Kalman filtering, one could have expected IMERG retrievals to be dramatically smoother than the radar reference at fine scales. Moreover, a similar analysis performed on the GPROF passive microwave instantaneous retrievals on which IMERG partially relies revealed that GPROF retrievals are significantly smoother than radar observations (Guilloteau et al. 2017). In contrast, only a marginal deficit of spectral energy is observed at scales 10 km–40 km for IMERG compared to

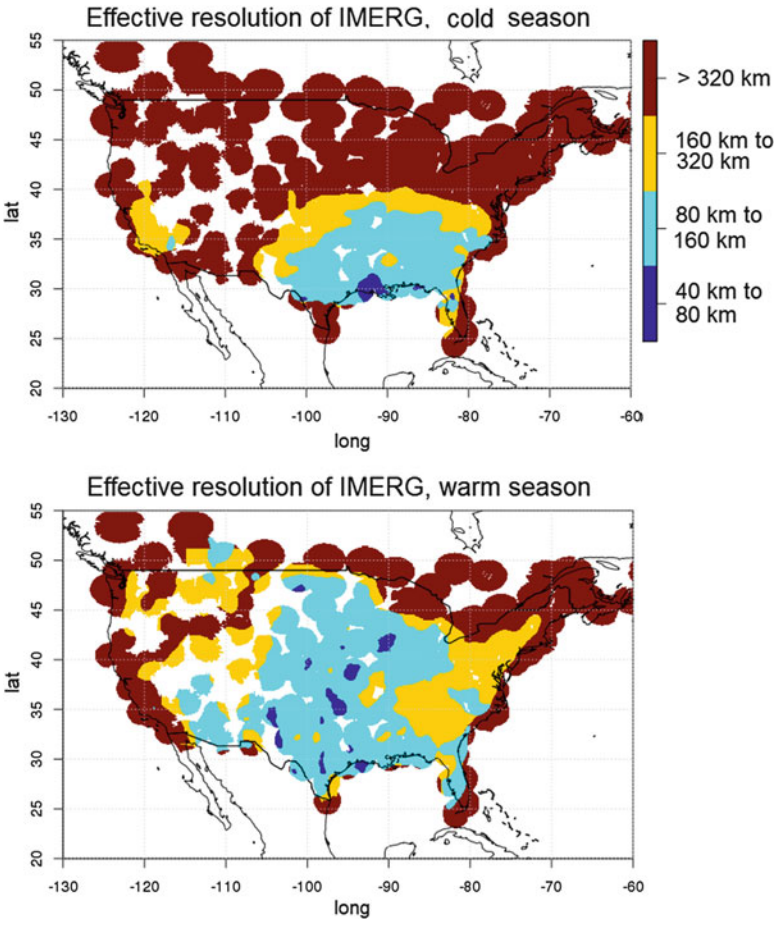

Fig. 29.8 Effective resolution of IMERG hourly precipitation evaluated against MRMS during the cold and warm seasons. The criterion (29.3) is used to define the effective resolution

MRMS. This may be partially due to the sampling variance introduced by the limited temporal frequency of the satellite observations. Indeed, while each MRMS hourly precipitation field is computed as the average of 30 instantaneous precipitation fields (one observation every 2 min), IMERG hourly precipitation is derived from only a few instantaneous satellite observations (2 infrared observations and no more than one or two microwave observations in 1 h).

In terms of mean squared error, it is more penalising to retrieve variations uncorrelated with the reference than to retrieve no variation at all at a given scale. This can be related to the concept of "double penalty" (Rossa et al. 2008; Mittermaier 2014), which states that mislocating a feature is more penalising than not detecting it in terms of mean squared error. Consequently, a filtering operation

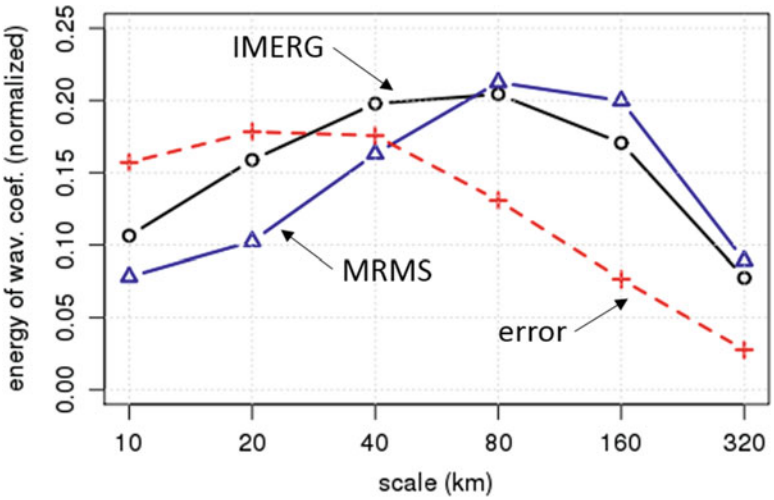

Fig. 29.9 Same as Fig. 29.4 for the cold season, but computed only over the South-Eastern region where the effective resolution is found finer than 160 km

reducing the fine-scale variability of IMERG would reduce the mean squared error (relatively to the MRMS reference) (Turner et al. 2004). However, this would produce unrealistically smooth fields. The suitability of such a filtering procedure depends of the targeted application; some applications such as, for example, rainfall-runoff modelling over a large basin, may tolerate mislocated fine-scale features better than others. Moreover, the smoothing of the fields would necessarily reduce the statistical variance and erase local extremes, which may have a considerable effect on the computed rainfall-runoff values for example (Harris et al. 2001; Smith et al. 2004; Nikolopoulos et al. 2010; Vergara et al. 2014).

The analysis of the spatial patterns is performed here at the hourly temporal scale. The poor ability of IMERG to resolve scales finer than 80 km at the hourly time scale does not mean that this product cannot resolve fine-scale patterns at longer time scales or resolve the fine-scale climatology. Indeed, the effective spatial resolution is expected to vary with the desired temporal resolution. Sampling-related noise in particular is expected to decrease at coarse time scales (Nijssen and Lettenmaier 2004; Gebremichael and Krajewski 2004). Figure 29.10 shows the effective resolution of IMERG evaluated against MRMS at the daily scale; the effective resolution is generally found to be improved by a factor of about two compared to the hourly scale. A comprehensive assessment would require performing the analysis at more temporal scales. Temporal averaging generally tends to reduce the fine-scale spatial variability, giving rise to smoother fields. However, some regions may still show strong climatic gradients at scales of a few km or a few dozen km (Hirose and Okada 2018). We note that, as well as for the spatial variations, a (one-dimensional) wavelet spectral analysis can be performed to assess the ability of a product to capture the

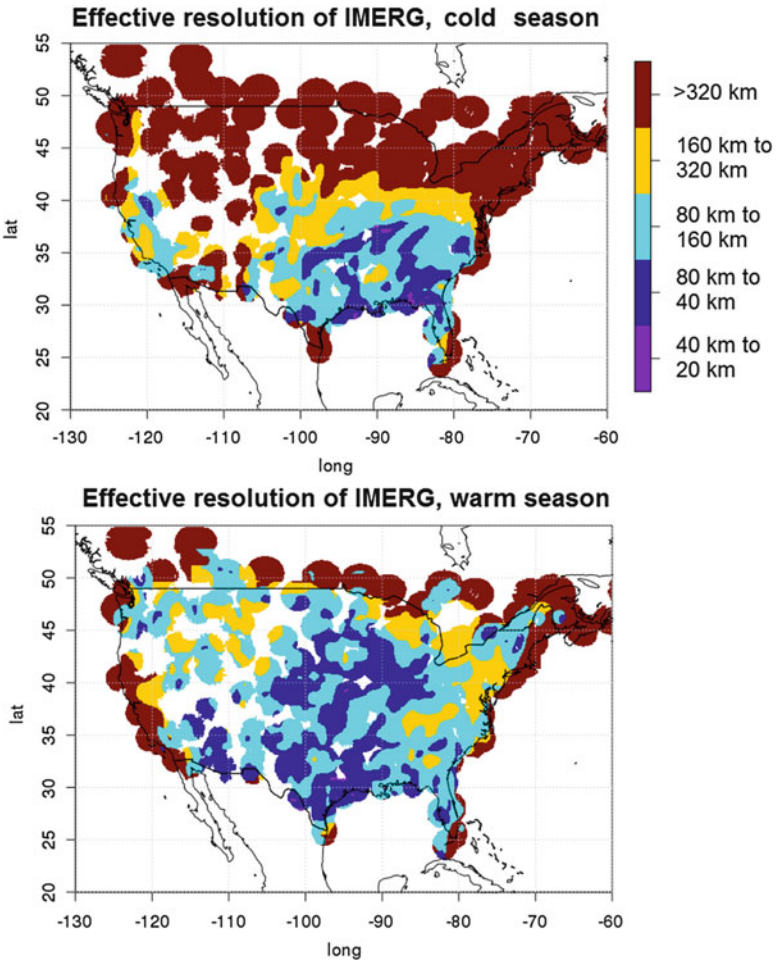

Fig. 29.10 Effective resolution of IMERG daily precipitation evaluated against MRMS during the cold and warm seasons. The criterion (29.3) is used to define the effective resolution

temporal variations of precipitation at a given location (Whitcher et al. 2000; De Jongh et al. 2006). One can also study the coupling between the temporal and spatial variations by performing successively the spatial and temporal wavelet decompositions (Guilloteau et al. 2016).

Acknowledgments This work was supported by the NASA Global Precipitation Measurement Program under Grants 80NSSC19K0684 and NNX16AO56G, and by NSF grants DMS-1839336 and ECCS-1839441. The wavelet decomposition procedure was implemented in R distributed under GNU General Public License, using the Waveslim 1.7.5 package (Whitcher 2015).

Appendix: Two-Dimensional Discrete Orthogonal Decomposition with the Haar Wavelet

Wavelets Functions in One Dimension and N Dimensions

In one-dimensional or multi-dimensional spaces, the wavelet transform is obtained through the convolution of the analysed signal with specific analysing functions called wavelets. Wavelets are locally oscillating functions; to be admitted as a wavelet a given function must meet several requirements such as having a zero mean and being square integrable (Kumar and Foufoula-Georgiou 1997; Mallat and Peyré 2008).

The function obtained by the dilation and/or translation of a wavelet is also a wavelet; multiple "daughter wavelets" can then be generated from a "mother wavelet", allowing multiscale analyses. In one dimension:

$$\psi_{a,b}(x) = a^{-\frac{1}{2}} \psi\left(\frac{x-b}{a}\right) \tag{29.4}$$

where $\psi_{a,\,b}$ is the daughter wavelet, ψ is the mother wavelet, $a \in \mathbb{R}$ is the dilation coefficient (or scale factor) and $b \in \mathbb{R}$ is the translation coefficient.

In N dimensions:

$$\psi_{a,\vec{\boldsymbol{B}}}\left(\vec{\boldsymbol{X}}\right) = a^{-\frac{1}{2^N}} \psi\left(\frac{\vec{\boldsymbol{X}} - \vec{\boldsymbol{B}}}{a}\right) \tag{29.5}$$

where $\vec{\boldsymbol{B}}$ is the translation vector belonging to $\mathbb{R}^N$.

The wavelet transform of the analysed function $y\left(\vec{\boldsymbol{X}}\right)$ is obtained by computing the inner products with the wavelets:

$$T\left(a, \vec{\boldsymbol{B}}\right) = \left\langle y, \psi_{a,\vec{\boldsymbol{B}}} \right\rangle = \int_{\mathbb{R}^N} y\left(\vec{\boldsymbol{X}}\right) \psi_{a,\vec{\boldsymbol{B}}}{}^{*}\left(\vec{\boldsymbol{X}}\right) d\vec{\boldsymbol{X}} \tag{29.6}$$

where T is the wavelet transform of y, * denotes the complex conjugate operator and $\langle\ \rangle$ denotes the canonical inner product of $L_2(\mathbb{R}^N)$.

The Haar Discrete Orthogonal Wavelets in One and Two Dimensions

In one dimension, the Haar mother wavelet is defined as:

$$\psi(x) = \begin{cases} 1 & if \;\; 0 \leq x < 0.5 \\ -1 & if \;\; 0.5 \leq x < 1 \\ 0 & otherwise \end{cases} \tag{29.7}$$

The Haar wavelet is associated to the smoothing function (or scaling function) ϕ:

$$\phi(x) = \begin{cases} 1 & if \;\; 0 \leq x < 1 \\ 0 & otherwise \end{cases} \tag{29.8}$$

ψ and ϕ are orthogonal functions as their inner product equals zero. As for the wavelet function, multiple smoothing functions $\phi_{a,\,b}$can be generated by dilatation and translation of ϕ (Eq. 29.4). While the wavelet ψ is a high-pass (H) convolution filter, the smoothing function ϕ is a low-pass (L) convolution filter.

By discretising the scaling and translation coefficients a and b, such as $a \in \{2^i, i \in \mathbb{Z}\}$ and $b \in \{k \times a, k \in \mathbb{Z}\}$ the ensemble of the Haar daughter wavelets $\{\psi_{a,\,b}\}$ forms an orthogonal basis of $L_2(\mathbb{R})$.

In two dimensions, the Haar wavelet and scaling functions are defined as follows:

$$\begin{aligned} \phi^{2D}(x_1, x_2) &= \phi(x_1)\phi(x_2) \\ \psi^{H}(x_1, x_2) &= \psi(x_1), \phi(x_2) \\ \psi^{V}(x_1, x_2) &= \phi(x_1), \psi(x_2) \\ \psi^{D}(x_1, x_2) &= \psi(x_1), \psi(x_2) \end{aligned}$$

ψ^H, ψ^V and ψ^D are the horizontal (HL), vertical (LH) and diagonal (HH) two-dimensional Haar wavelets. $\phi^{2D}$is the two-dimensional Haar smoothing (LL) function. The four functions are graphically represented in Fig. 29.11.

The ensemble of the two-dimensional Haar wavelets $\left\{\psi^H_{a,\vec{\boldsymbol{B}}}, \psi^V_{a,\vec{\boldsymbol{B}}}, \psi^D_{a,\vec{\boldsymbol{B}}}\right\}$ with $a \in \{2^i, i \in \mathbb{Z}\}$ and $\vec{\boldsymbol{B}} \in \left\{\vec{\boldsymbol{k}} \times a, \vec{\boldsymbol{k}} \in \mathbb{Z}2\right\}$ forms an orthogonal basis of $L_2(\mathbb{R}^2)$. The decomposition of a two-dimensional precipitation field in this basis is illustrated in Fig. 29.12.

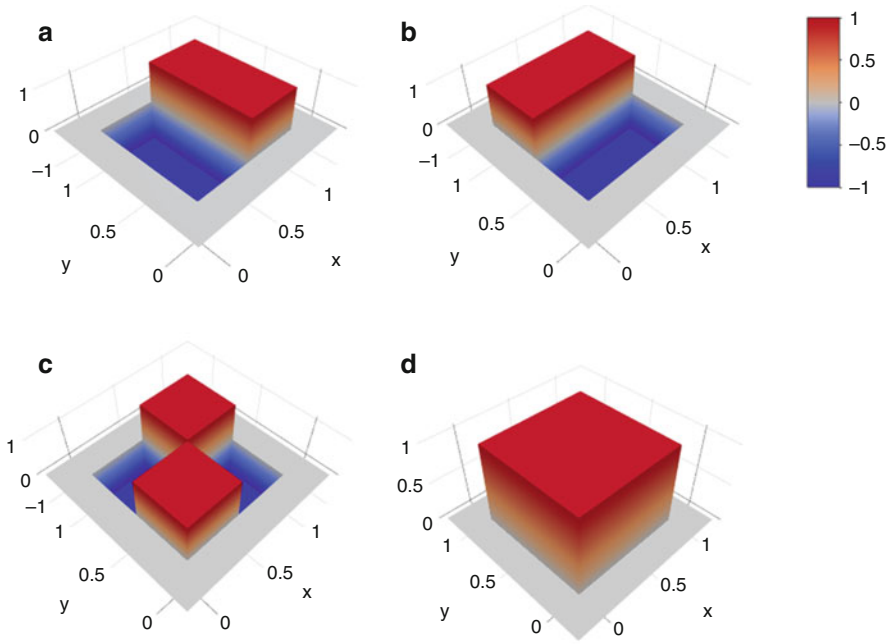

Fig. 29.11 Representation of the spatial convolution filters used to perform the two-dimensional Haar wavelet decomposition. A and B and C are the wavelet functions ψ^H, ψ^V and ψ^D used to compute the horizontal (HL), vertical (LH) and diagonal (HH) wavelet coefficients. D is the smoothing function ϕ^{2D} used to compute the smoothing (LL) coefficients. The four functions are orthogonal, meaning that the scalar product of one with any of the other three equals zero

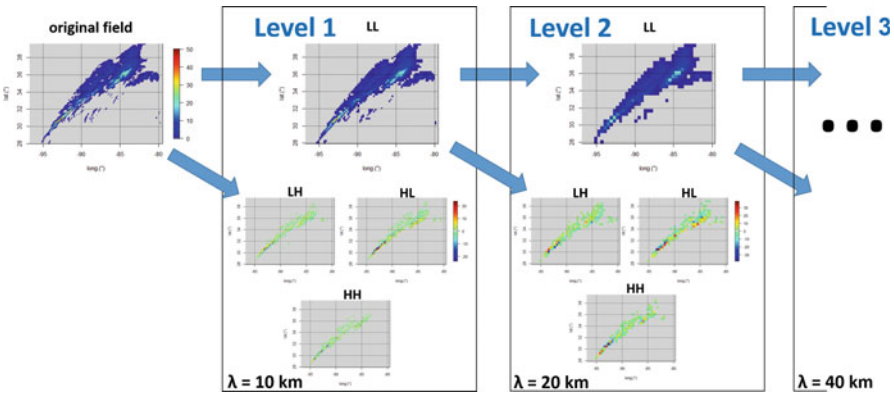

Fig. 29.12 Illustration of the discrete wavelet decomposition process of a two-dimensional field (using the Haar wavelet)

References

Bousquet, O., Lin, C. A., & Zawadzki, I. (2006). Analysis of scale dependence of quantitative precipitation forecast verification: A case-study over the Mackenzie river basin. *Quarterly Journal of the Royal Meteorological Society, 132*, 2107–2125. https://doi.org/10.1256/qj.05.154.

De Jongh, I. L., Verhoest, N. E., & De Troch, F. P. (2006). Analysis of a 105-year time series of precipitation observed at Uccle, Belgium. *International Journal of Climatology, 26*, 2023–2039. https://doi.org/10.1002/joc.1352.

Frehlich, R., & Sharman, R. (2008). The use of structure functions and spectra from numerical model output to determine effective model resolution. *Monthly Weather Review, 136*, 1537–1553. https://doi.org/10.1175/2007MWR2250.1.

Gebremichael, M., & Krajewski, W. F. (2004). Characterization of the temporal sampling error in space-time-averaged rainfall estimates from satellites. *Journal of Geophysical Research, 109* (D11), D11110. https://doi.org/10.1029/2004JD004509.

Grasso, L. D. (2000). The differentiation between grid spacing and resolution and their application to numerical modeling. *Bulletin of the American Meteorological Society, 81*(3), 579. https://doi.org/10.1175/1520-0477(2000)081<0579:CAA>2.3.CO;2.

Guilloteau, C., Roca, R., & Gosset, M. (2016). A multiscale evaluation of the detection capabilities of high-resolution satellite precipitation products in West Africa. *Journal of Hydrometeorology, 17*(7), 2041–2059. https://doi.org/10.1175/JHM-D-15-0148.1.

Guilloteau, C., Foufoula-Georgiou, E., & Kummerow, C. D. (2017). Global multiscale evaluation of satellite passive microwave retrieval of precipitation during the TRMM and GPM eras: Effective resolution and regional diagnostics for future algorithm development. *Journal of Hydrometeorology, 18*(11), 3051–3070. https://doi.org/10.1175/JHM-D-17-0087.1.

Haile, A. T., Habib, E., & Rientjes, T. (2013). Evaluation of the Climate Prediction Center (CPC) morphing technique (CMORPH) rainfall product on hourly time scales over the source of the Blue Nile River. *Hydrological Processes, 27*(12), 1829–1839. https://doi.org/10.1002/hyp.9330.

Harris, D., Foufoula-Georgiou, E., Droegemeier, K. K., & Levit, J. J. (2001). Multiscale statistical properties of a high-resolution precipitation forecast. *Journal of Hydrometeorology, 2*(4), 406–418. https://doi.org/10.1175/1525-7541(2001)002<0406:MSPOAH>2.0.CO;2.

Hirose, M., & Okada, K. (2018). A 0.01 degree resolving TRMM PR precipitation climatology. *Journal of Applied Meteorology and Climatology, 57*, 1645–1661. https://doi.org/10.1175/JAMC-D-17-0280.1.

Hong, Y., Hsu, K.-L., Sorooshian, S., & Gao, X. (2004). Precipitation estimation from remotely sensed imagery using an artificial neural network cloud classification system. *Journal of Applied Meteorology and Climatology, 43*(12), 1834–1853. https://doi.org/10.1175/JAM2173.1.

Hossain, F., & Anagnostou, E. N. (2006). A two-dimensional satellite rainfall error model. *IEEE Transactions on Geoscience and Remote Sensing, 44*(6), 1511–1522. https://doi.org/10.1109/TGRS.2005.863866.

Hossain, F., & Huffman, G. J. (2008). Investigating error metrics for satellite rainfall data at hydrologically relevant scales. *Journal of Hydrometeorology, 9*(3), 563–575. https://doi.org/10.1175/2007JHM925.1.

Huffman, G. J., Bolvin, D. T., Braithwaite, D., Hsu, K., Joyce, R., Kidd, C., Nelkin, E. J., & Xie, P. (2015). *NASA global precipitation measurement (GPM) integrated multi-satellitE retrievals for GPM (IMERG)*. Algorithm Theoretical Basis Doc., v4.5, 26 pp. Available at https://pmm.nasa.gov/sites/default/files/document_files/IMERG_ATBD_V4.5.pdf. Last accessed 27 Oct 2018.

Joyce, R. J., & Xie, P. (2011). Kalman filter–based CMORPH. *Journal of Hydrometeorology, 12* (6), 1547–1563. https://doi.org/10.1175/JHM-D-11-022.1.

Kumar, P. (1995). A wavelet based methodology for scale-space anisotropic analysis. *Geophysical Research Letters, 22*(20), 2777–2780. https://doi.org/10.1029/95GL02934.

Kumar, P., & Foufoula-Georgiou, E. (1993). A multicomponent decomposition of spatial rainfall fields: 1. Segregation of large-and small-scale features using wavelet transforms. *Water Resources Research, 29*(8), 2515–2532. https://doi.org/10.1175/JHM-D-11-022.1.

Kumar, P., & Foufoula-Georgiou, E. (1997). Wavelet analysis for geophysical applications. *Reviews of Geophysics, 35*(4), 385–412. https://doi.org/10.1029/97RG00427.

Kummerow, C. D., Randel, D. L., Kulie, M., Wang, N.-Y., Ferraro, R. R., Munchak, S. J., & Petkovic, V. (2015). The evolution of the Goddard profiling algorithm to a fully parametric scheme. *Journal of Atmospheric and Oceanic Technology, 32*, 2265–2280. https://doi.org/10.1175/JTECH-D-15-0039.1.

Labat, D. (2005). Recent advances in wavelet analyses: Part 1. A review of concepts. *Journal of Hydrology, 314*(1–4), 275–288. https://doi.org/10.1016/j.jhydrol.2005.04.003.

Labat, D., Ronchail, J., & Guyot, J. L. (2005). Recent advances in wavelet analyses: Part 2—Amazon, Parana, Orinoco and Congo discharges time scale variability. *Journal of Hydrology, 314*(1–4), 289–311. https://doi.org/10.1016/j.jhydrol.2005.04.004.

Mallat, S., & Peyré, G. (2008). Time meets frequency. In *A wavelet tour of signal processing: The sparse way* (pp. 89–150). Boston: Academic. ISBN: 0123743702.

Mittermaier, M. P. (2014). A strategy for verifying near-convection-resolving model forecasts at observing sites. *Weather and Forecasting, 29*(2), 185–204. https://doi.org/10.1175/WAF-D-12-00075.1.

Nijssen, B., & Lettenmaier, D. P. (2004). Effect of precipitation sampling error on simulated hydrological fluxes and states: Anticipating the global precipitation measurement satellites. *Journal of Geophysical Research, 109*(D2), D02103. https://doi.org/10.1029/2003JD003497.

Nikolopoulos, E. I., Anagnostou, E. N., Hossain, F., Gebremichael, M., & Borga, M. (2010). Understanding the scale relationships of uncertainty propagation of satellite rainfall through a distributed hydrologic model. *Journal of Hydrometeorology, 11*(2), 520–532. https://doi.org/10.1175/2009JHM1169.1.

Perica, S., & Foufoula-Georgiou, E. (1996). Model for multiscale disaggregation of spatial rainfall based on coupling meteorological and scaling descriptions. *Journal of Geophysical Research, 101*(D21), 26347–26361. https://doi.org/10.1029/96JD01870.

Petty, G. W. (2018). On some shortcomings of Shannon entropy as a measure of information content in indirect measurements of continuous variables. *Journal of Atmospheric and Oceanic Technology, 35*(5), 1011–1021. https://doi.org/10.1175/JTECH-D-17-0056.1.

Pielke, R. A. (1991). A recommended specific definition of "resolution". *Bulletin of the American Meteorological Society, 72*(12), 1914–1914. https://doi.org/10.1175/1520-0477-72.12.1914.

Rios Gaona, M. F., Overeem, A., Leijnse, H., & Uijlenhoet, R. (2016). First-year evaluation of GPM rainfall over the Netherlands: IMERG day 1 final run (V03D). *Journal of Hydrometeorology, 17*, 2799–2814. https://doi.org/10.1175/JHM-D-16-0087.1.

Rossa, A., Nurmi, P., & Ebert, E. E. (2008). Overview of methods for the verification of quantitative precipitation forecasts. In S. C. Michaelides (Ed.), *Precipitation: Advances in measurement, estimation and prediction* (pp. 419–452). Berlin/Heidelberg: Springer. ISBN: 978-3-540-77655-0.

Scheel, M. L. M., Rohrer, M., Huggel, C., Santos Villar, D., Silvestre, E., & Huffman, G. J. (2011). Evaluation of TRMM multi-satellite precipitation analysis (TMPA) performance in the Central Andes region and its dependency on spatial and temporal resolution. *Hydrology and Earth System Sciences, 15*(8), 2649–2663. https://doi.org/10.5194/hess-15-2649-2011.

Shen, Y., Xiong, A., Wang, Y., & Xie, P. (2010). Performance of high-resolution satellite precipitation products over China. *Journal of Geophysical Research, 115*(D2), D02114. https://doi.org/10.1029/2009JD012097.

Skamarock, W. C. (2004). Evaluating mesoscale NWP models using kinetic energy spectra. *Monthly Weather Review, 132*(12), 3019–3032. https://doi.org/10.1175/MWR2830.1.

Smith, M. B., Koren, V. I., Zhang, Z., Reed, S. M., Pan, J. J., & Moreda, F. (2004). Runoff response to spatial variability in precipitation: An analysis of observed data. *Journal of Hydrology, 298* (1–4), 267–286. https://doi.org/10.1016/j.jhydrol.2004.03.039.

Sohn, B. J., Han, H. J., & Seo, E. K. (2010). Validation of satellite-based high-resolution rainfall products over the Korean peninsula using data from a dense rain gauge network. *Journal of Applied Meteorology and Climatology, 49*(4), 701–714. https://doi.org/10.1175/2009JAMC2266.1.

Starck, J. L., Murtagh, F., & Gastaud, R. (1998). A new entropy measure based on the wavelet transform and noise modeling. *IEEE Transactions Circuits and Systems-II: Analog and Digital Signal Processing, 45*(8), 1118–1124. https://doi.org/10.1109/82.718822.

Turk, F. J., Sohn, B. J., Oh, H. J., Ebert, E. E., Levizzani, V., & Smith, E. A. (2009). Validating a rapid-update satellite precipitation analysis across telescoping space and time scales. *Meteorology and Atmospheric Physics, 105*(1–2), 99–108. https://doi.org/10.1007/s00703-009-0037-4.

Turner, B. J., Zawadzki, I., & Germann, U. (2004). Predictability of precipitation from continental radar images. Part III: Operational nowcasting implementation (MAPLE). *Journal of Applied Meteorology, 43*(2), 231–248. https://doi.org/10.1175/1520-0450(2004)043<0231:POPFCR>2.0.CO;2.

Vasić, S., Lin, C. A., Zawadzki, I., Bousquet, O., & Chaumont, D. (2007). Evaluation of precipitation from numerical weather prediction models and satellites using values retrieved from radars. *Monthly Weather Review, 135*(11), 3750–3766. https://doi.org/10.1175/2007MWR1955.1.

Vergara, H., Hong, Y., Gourley, J. J., Anagnostou, E. N., Maggioni, V., Stampoulis, D., & Kirstetter, P.-E. (2014). Effects of resolution of satellite-based rainfall estimates on hydrologic modeling skill at different scales. *Journal of Hydrometeorology, 15*(2), 593–613. https://doi.org/10.1175/JHM-D-12-0113.1.

von Storch, H. (1999). Misuses of statistical analysis in climate research. In H. von Storch & A. Navarra (Eds.), *Analysis of climate variability* (pp. 11–26). Berlin/Heidelberg: Springer. https://doi.org/10.1007/978-3-662-03167-4_2.

Weniger, M., Kapp, F., & Friederichs, P. (2017). Spatial verification using wavelet transforms: A review. *Quarterly Journal of the Royal Meteorological Society, 143*(702), 120–136. https://doi.org/10.1002/qj.2881.

Whitcher, B. (2015). Waveslim: Basic wavelet routines for one-,two- and three-dimensional signal processing, version 1.7.5. R package. [Available at https://cran.r-project.org/web/packages/waveslim/index.html, last accessed 30 Nov 2018].

Whitcher, B., Guttorp, P., & Percival, D. B. (2000). Wavelet analysis of covariance with application to atmospheric time series. *Journal of Geophysical Research, 105*(D11), 14941–14962. https://doi.org/10.1029/2000JD900110.

Wong, M., & Skamarock, W. C. (2016). Spectral characteristics of convective-scale precipitation observations and forecasts. *Monthly Weather Review, 144*(11), 4183–4196. https://doi.org/10.1175/MWR-D-16-0183.1.

Zhang, J., Howard, K., Langston, C., Kaney, B., Qi, Y., Tang, L., Grams, H., Wang, Y., Cocks, S., Martinaitis, S., Arthur, A., Cooper, K., Brogden, J., & Kitzmiller, D. (2016). Multi-radar multi-sensor (MRMS) quantitative precipitation estimation: Initial operating capabilities. *Bulletin of the American Meteorological Society, 97*, 621–638. https://doi.org/10.1175/BAMS-D-14-00174.1.